

## **Error Characteristics of GPS Retrieved Refractivity Using a Simulation Study**

**Shu-Hua CHEN**

*Department of Land, Air, and Water Resources, University of California, Davis, California, USA*

**Francois VANDENBERGHE**

*National Center for Atmospheric Research, Boulder, Colorado, USA*

**and**

**Ching-Yuang HUANG**

*Department of Atmospheric Sciences, National Central University, Chung-Li, Taiwan*

*(Manuscript received 14 July 2005, in final form 13 February 2006)*

### **Abstract**

A simulation study was designed to investigate the error characteristics of retrieved local refractivity arising only from the assumption of spherical symmetry. The convergence of error estimation with respect to different horizontal resolutions was examined, and a resolution higher than 30 km was found to be reasonable for this simulation study.

Two cases, one in summer 1997 and the other in winter 1998, were used to study errors of retrieved local refractivity. The error can reach 10 units in the lower troposphere under the assumption of spherical symmetry. Error decreases with height linearly, until about 3 km and then dramatically above 3 km. A local maximum error occurs at approximately 6 km in the 1997 case because there were large refractivity disturbances on the lee side of the Rocky Mountains around that level.

The level of the maximum error over land ( $\sim 2\text{--}3$  km) was higher than over ocean ( $\sim 1$  km) due to complex topography, as well as a deeper boundary layer over land. As a result, the average root mean square error below 3 km presents a meandering feature over the entire domain of interest. Moreover, the error close to the surface over ocean was slightly higher than that over land. However, in the 2–4 km range the error was slightly lower over ocean than over land. Note that the altitude of maximum error over ocean can be shifted upward when strong disturbances, such as severe weather, exist over the region. The error during summer was larger than that during winter, and it was greater at lower latitudes than at higher latitudes, as reported in previous studies.

When modeling retrieved local refractivity, the observational error is a function of the model horizontal resolution. The error was reduced as model resolution was decreased, but there was a lower limit for an optimal resolution. This optimal resolution in the lower atmosphere was higher ( $\sim 190$  km) than that in the middle and upper atmosphere ( $\sim 250$  km) in this study, due to a stronger vertical gradient of refractivity and higher vertical resolution in the lower troposphere.

---

Corresponding author: Shu-Hua Chen, Department of Land, Air, and Water Resources, University of California, Davis, California 95616-8627, USA.

E-mail: shachen@ucdavis.edu.

© 2006, Meteorological Society of Japan

### **1. Introduction**

A radio occultation observation occurs whenever a Low Earth Orbit (LEO) satellite rises or

sets relative to one of the Global Positioning System (GPS) satellite constellation (Kursinski et al. 1997). As a path, or ray, follows the electromagnetic waves travelling from the occulting GPS satellite to the LEO, it is tangent to the Earth ellipsoid at a location called the perigee point (tangent point), which is also the point on the ray path closest to the Earth. The continuous emission of an electromagnetic signal combined with the satellites' motions creates an occultation, which is comprised of many rays.

The Constellation Observing System for Meteorology, Ionosphere and Climate (COSMIC, <http://cosmic.cosmic.ucar.edu>) project will launch six LEOs in March 2006. The coverage of the radio occultation data from the COSMIC project was optimized, and the time latency for data availability will potentially meet operational requirements (within 2–3 hours of the observations). Daily it will deliver ~2500 profiles of meteorological data, from a height of 40 km, to near the surface (personal communication with Drs. Bill Kuo and Doug Hunt at NCAR). The rays within the occultation planes implicitly contain atmospheric information, such as moisture, temperature, and barometric pressure. Therefore, COSMIC will provide a source of weather observations that can be potentially used for global weather forecasting and long-term climate study.

Various types of radio occultation products, such as excess phase, bending angle, refractivity, and temperature and moisture, can be used to improve weather analysis, simulations, or forecasts (Eyre 1994; Kuo et al. 2000). The retrieved temperature and moisture (Healy and Eyre 2000; Palmer et al. 2000; Hajj et al. 2002; Poli et al. 2002) are in the format closest to model variables, and the assimilation of these data is straightforward and computationally efficient. However, their quality in the lower troposphere, the primary region of interest for severe weather, has been a concern. Refractivity (Rocken et al. 1997; Hajj et al. 2002; Kuo et al. 2004), the next closest to atmospheric numerical model variables, has slightly better quality since fewer assumptions are made for retrievals, when compared with temperature and moisture. The assimilation of local refractivity is reasonably simple and efficient, and has been used more often in meteorology (Zou et al. 1995; Kuo et al. 1997; Healy et al. 2005; Huang et al. 2005). With an Observing System Simulation Experiment approach, Kuo et al. (1997) showed the positive impact of assimilating retrieved local refractivity data on modeling an extratropical cyclone. Healy et al. (2005) further demonstrated the improvement of temperature forecasts in the upper troposphere and lower stratosphere, in particular for the southern hemisphere, after the assimilation of CHALLENGING Minisatellite Payload (CHAMP) GPS local refractivity, using the Met Office numerical weather prediction system.

Using a more sophisticated approach, Zou et al. (1999) and Zou et al. (2000) directly assimilated bending angles, which are close to raw measurements, and have smaller errors than retrieved refractivity. Although results from their studies are promising, the assimilation of bending angles is quite expensive in the computing cost. The limitation of computational resources and the timing desired for issuing forecasts encourage a more economical approach, especially after more radio occultation data become available from the COSMIC project. As a more efficient alternative to the assimilation of bending angles, Syndergaard et al. (2005) and Sokolovskiy et al. (2005) recently developed a new methodology, using a linearized observational operator (non-local refractivity operator) to assimilate the observed refractivity. The fractional errors of these new observables are one order of magnitude smaller than those of local refractivity. Moreover, no meteorological information outside the regional model domain is required. Although results from this new methodology are very encouraging, further evidence from real case studies is required.

When data are assimilated, assimilation results depend critically on observational error variances. Different methodologies have been applied to estimate observational errors (Xu et al. 2001; Xu and Li 2001; Healy 2001; Zou 2002; Seemann et al. 2003; Kuo et al. 2004; Poli and Joiner 2004; Sokolovskiy et al. 2005; Syndergaard et al. 2005). Innovation vectors (i.e., observation—background) can be used to estimate the observation errors if: (i) the forecast errors are known; (ii) observation errors are independent of forecast errors; and (iii) the observations are spatially isotropic and uncor-

related. This method has been widely implemented (Hollingsworth and Lonnberg 1986; Lonnberg and Hollingsworth 1986; Xu et al. 2001; Xu and Li 2001; Kuo et al. 2004), but is only valid for regions of sufficiently dense observation coverage. Kuo et al. (2004) studied the error of retrieved local refractivity using innovation vectors with available radiosondes and coarse-resolution global reanalysis. Temporal and spatial interpolation, which can introduce extra error, is unavoidable in their approach because of the limited amount of available GPS data. Another approach is to use reliable or well characterized observations to estimate the error of a new observation (Seemann et al. 2003); however, it requires a large number of observations. In addition, frequent sampling from a dense set of locations is needed to minimize temporal and spatial interpolation errors.

A small number of radio occultation observations from a sparse observational network is available, and the sites are often not closely collocated with the upper air soundings (i.e., radiosondes), which are used as ground-truth for meteorological data estimates. Moreover, there are not many conventional observations available over oceans. Therefore, it has been relatively difficult to study error characteristics of radio occultation observables using other observations, and simulation studies have been often used (Zou et al. 1999; Healy 2001; Zou et al. 2002; Poli and Joiner 2004; Sokolovskiy et al. 2005; Syndergaard et al. 2005). Zou et al. (1999) developed a ray-tracing code, which was applied to estimate errors of local refractivity, using coarse-resolution National Centers for Environmental Prediction (NCEP) 62-wave (approximately  $1.9^\circ \times 1.9^\circ$ ) global reanalysis. Using the same global data source, the average fractional error of bending angles, due to the assumption of spherical symmetry, was further estimated by Zou et al. (2002). The error from their study is less than 0.15%, which is negligible, since the coarse-resolution reanalysis data are used. In contrast, Healy (2001) used high-resolution mesoscale model forecast data ( $12 \text{ km} \times 12 \text{ km}$ ) to demonstrate that the statistical error in the bending angle can reach 3–4% in the lower troposphere, including error due to perpendicular refractive index gradient, which is non-negligible. In the same study,

Healy (2001) also illustrated that the averaged error of the impact parameter can reach 73 m. Sokolovskiy et al. (2005) applied a linearized non-local refractivity operator to study the fractional error of radio occultation observables, using 4 km two-dimensional mesoscale simulations.

Here we study the error characteristics of retrieved local refractivity using high-resolution mesoscale numerical simulations. While different components of the errors in the retrieval processes have been studied, as mentioned above, the goal of this study is to investigate the error of retrieved local refractivity resulting only from the assumption of spherical symmetry in the Abelian inversion algorithm.

In this study, an ideal atmosphere was created and was treated as an arbitrary one, assuming that the model resolution is adequate and the atmospheric inhomogeneity is reasonably represented. Utilizing this ideal atmosphere, the ray tracing code was applied to simulate bending angles, which were then used to retrieve local refractivity. As a result, the error of retrieved local refractivity due to the assumption of spherical symmetry in the Abelian retrieval algorithm can be obtained by comparing its value with the refractivity computed from the ideal atmosphere. The representativeness of an ideal atmosphere (e.g., inhomogeneity and reality of an atmosphere), and the accuracy of the operator (i.e., the ray tracing code) play important roles in this study. In other words, to obtain reasonable results, the error contributed by the operator itself should be much smaller than the error from the retrieval algorithm. The ray-tracing code based on Zou et al. (1999) is quite accurate and is applied to a high-resolution regional model in this study. This paper is organized as follows. The ray tracing operator and the methodology are described in Section 2. Three experiments are designed and their results are discussed in Section 3, and a summary is given in Section 4.

## 2. Ray tracing model and methodology

### 2.1 Description of ray tracing model

The basic measurement of the GPS occultation is the frequency, or Doppler shift, between the emitted signal from the occulting GPS satellite and the received signal by the LEO. With some approximations, Snell's law (Kursinski et

al. 1997) can be applied to estimate the vertical distribution of the bending angles (the difference between the directions of the ray at receptor and emitter) from the Doppler shift. Following Zou et al. (1999), our modeling approach does not derive the bending angle from the observed Doppler shift, but directly from the geometry of the ray (i.e., by ray-tracing techniques). This approximation was studied by Zou et al. (2002) using coarse-resolution reanalysis and the error is less than 0.15%, which is much smaller than that from Healy (2001) using high-resolution model forecast data. Provided that the atmospheric refractivity field is known, the second order differential equation can be numerically integrated and the corresponding ray path constructed step by step, hence the name ray-tracing.

The ray-tracing code was adapted from the previous work of Zou et al. (1999) with the modifications described in Liu and Zou (2003). The same spatial interpolation packages were used, and the code was modified to accommodate the regional model map projections. Gridded atmospheric refractivity fields ( $N$ ), which were interpolated horizontally using a bilinear method and vertically using a cubic spline method along the ray path, were computed from the model gridded pressure, temperature and water vapor pressure using the relation:

$$N = \underbrace{c_1 \frac{P}{T}}_{\text{dry}} + \underbrace{c_2 \frac{e}{T^2}}_{\text{wet}}, \quad (1)$$

where  $P$  is pressure (hPa),  $T$  is temperature (K), and  $e$  is water vapor pressure (hPa).  $c_1$  ( $= 77.6 \text{ K/hPa}$ ) and  $c_2$  ( $= 3.73 \times 10^5 \text{ K}^2/\text{hPa}$ ) are constants. Contributions from the dry atmosphere (i.e., dry refractivity) and the moist atmosphere (i.e., wet refractivity) are indicated in Eq. 1. For a given occultation, integration begins at the tangent points and proceeds toward the GPS and LEO satellites. To simplify the configuration, tangent points are assumed to be vertically aligned and regularly spaced, and the azimuth angles of the rays are assumed to be the same. Under these assumptions, all tangent points will project onto the same point on the Earth's surface, referred to as the occultation point. An occultation is, therefore, characterized by the latitude and longitude of the

occultation point, the vertical spacing of the tangent points, and the azimuth angle of the occultation plane.

As demonstrated in Poli and Joiner (2004), the percentage errors of bending angle and retrieved refractivity resulting from the neglect of the tangent point drift (TPD) in a GPS observation operator can reach 0.4 to 1.2%, and 0.3 to 0.7%, respectively, and larger values are usually evident for the stratosphere. Although the TPD cannot be taken into account here due to our configuration and assumptions, errors estimated from Poli and Joiner (2004), as well as those from other retrieval algorithms (e.g., Healy 2001), can be incorporated with results from this study to count for total errors of retrieved local refractivity.

## 2.2 Methodology: a simulation study

The procedure for estimating the error of retrieved local refractivity comprises several steps. The flow chart is shown in Fig. 1a. First, an ideal atmosphere was constructed. To reproduce inhomogeneities in the lower atmosphere, the 5<sup>th</sup> Version of the Penn State/NCAR Mesoscale Model (MM5; Grell et al. 1994) was used to create a set of high-resolution data. Due to the limited vertical and horizontal region of the MM5 domain, climatological data from the COSPAR International Reference Atmosphere (CIRA) were used to compute the refractivity field whenever the ray passes out of the MM5 domain (Fig. 1b). CIRA data consist of latitudinal monthly means of pressure and temperature given every 5 km in the vertical from 0 to 120 km and every 5 degrees in the horizontal. In this study, a smooth transition between the MM5 and CIRA refractivity field was applied in the 10 km to 20 km transition zone, to avoid unrealistic vertical refractivity gradients.

Secondly, given an occultation configuration (i.e., latitude and longitude of the occultation point, the vertical spacing of the tangent points, and the azimuth angle of the occultation plane), the ideal atmosphere was used to simulate bending angles up to the top of the atmosphere using the ray-tracing operator described in Section 2.1. In this study, rays were assumed to be travelling from North to South for a zero azimuth angle, and from East to West for a 90° azimuth angle direction. As mentioned earlier, to simplify the problem, all rays that define an

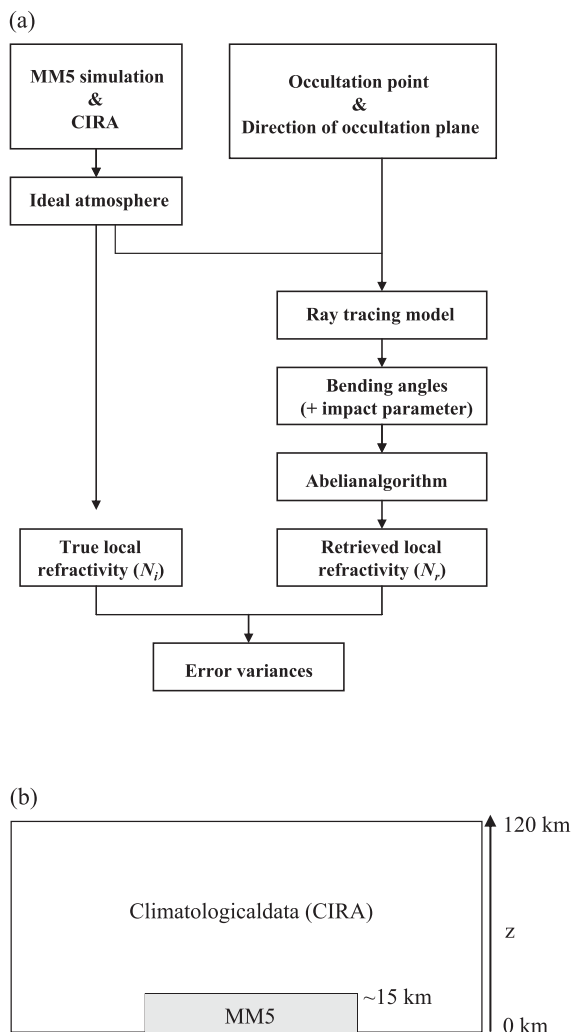


Fig. 1. (a) The flow chart of the simulation study, and (b) a schematic diagram for an ideal atmosphere which consists of a high-resolution region from an MM5 simulation and coarse-resolution elsewhere from climatological data (i.e., CIRA).  $N_i$  is the local refractivity derived from ideal atmosphere, while  $N_r$  is retrieved refractivity.

occultation were assumed to be in the same plane (i.e., occultation plane), with all tangent points vertically aligned every 300 m above the occultation point. In addition to bending angles, impact parameters (i.e., the radius of the tangent point multiplied by the local refractive index) at tangent points were also computed. Note that the value of the impact parameter at the tangent point cannot be derived from obser-

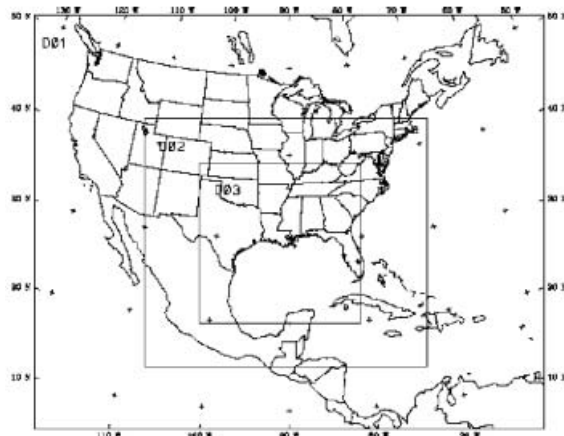


Fig. 2. MM5 domains for experiment 1 with resolutions of 90, 30, and 10 km for domains 1, 2, and 3, respectively.

ventions. Therefore, errors can be introduced due to this assumption.

Thirdly, under the assumption that the atmosphere is spherically symmetrical (Kursinski et al. 1997), the refractivity,  $N_r$ , was then retrieved with the Abelian inversion algorithm from the bending angles and impact parameters simulated from the ideal refractivity field, based on MM5 and CIRA ( $N_i$ ). To statistically estimate the error of retrieved refractivity resulting from the Abelian inversion under the assumption of spherical symmetry, many occultation planes were chosen. Finally, the standard deviation of the retrieved local refractivity error ( $\sigma_o$ ) was calculated using the formula:

$$\sigma_o = \sqrt{\frac{1}{M} \sum_{k=1}^M (N_{i,k} - N_{r,k})^2}, \quad (2)$$

where  $M$  is the number of occultation samples.

### 3. Experiments and results

#### 3.1 Experiment 1: Sensitivity of the model horizontal resolution to the convergence of error estimation

##### 3.1.a. Experiment design

In order to make a reasonable estimate of error characteristics and variances, the representation of the inhomogeneity in the ideal atmosphere is important. With our current computer resources, it was impossible to use an extremely high resolution (e.g.,  $\sim 1$  km) for a large domain MM5 simulation. Therefore, de-

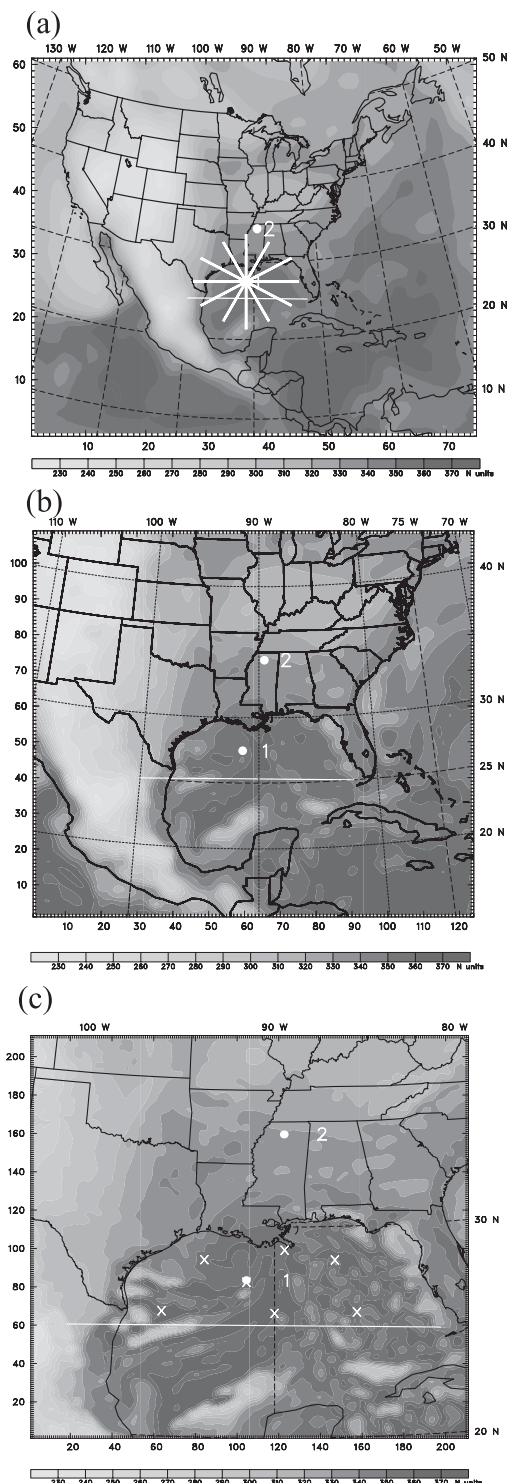


Fig. 3. MM5 24-h simulated total refractivity at 950 hPa from domains (a) 1, (b) 2, and (c) 3 for experiment 1. Occultation points 1 and 2 are selected for the convergence test of the model reso-

lution. Each point has 12 occultation planes (every  $30^\circ$ ) as shown in (a). The lines in (a), (b), and (c) refer to the vertical cross-sections in Fig. 4. The 7 cross points in (c) apply to experiment 3.

termination of the MM5 model resolution that is acceptable to achieve the objectives of this study was important.

Experiment 1 was designed to examine the convergence of refractivity error estimation, instead of refractivity itself, with respect to different model resolutions. Three domains (81 km, 27 km, and 9 km; Fig. 2), with a two-way nesting, were used for MM5 simulations with the initial time at 0000 UTC July 17 1997. The grid's dimensions were  $75 \times 61 \times 30$ ,  $124 \times 109 \times 30$ , and  $211 \times 211 \times 30$  in x-y- $\sigma$  directions in domains 1, 2, and 3, respectively. The vertical resolution was the same for all three domains, and was stretched up to 100 hPa. To improve the accuracy of the inhomogeneity of the initial conditions, the Special Sensor Microwave/Imager (SSM/I) radiances were assimilated. Reanalysis from the NCEP Global Data Assimilation System (GDAS) was used for the first-guess of the MM5 3D variational data assimilation system (3DVAR). As used in Chen et al. (2004), the standard deviation of SSM/I radiances errors were 3.0 K, 3.0 K, 4.33 K, 5.65 K, 5.65 K, 7.0 K, and 7.0 K for channels 19V, 19H, 22V, 37V, 37H, 85V, and 85H, respectively, where H indicates horizontal polarization, and V indicates vertical polarization. The corresponding numbers present the integer portion of the frequencies (i.e., 19.3 GHz, 22.2 GHz, 37.0 GHz, and 85.5 GHz). Details of the assimilation of SSM/I radiances are given in Chen et al. (2004). Since the resolution of the NCEP GDAS reanalysis is relatively coarse ( $2.5^\circ \times 2.5^\circ$ ), MM5 was integrated for 24 hours (i.e., until 0000 UTC 18 July), during which time the representation of inhomogeneities in the atmospheric refractivity field was improved. The time step for domain 1 was 240 seconds.

Figure 3 shows that the 24-h simulation result from domain 3, with a resolution of 10 km, had more fine-scale structures than those from domain 1, with a resolution of 90 km. Although the fine-scale structures from domain 2 were

smoother, the pattern remained. This was also clearly shown in the vertical cross sections of the simulated water vapor mixing ratio in Fig. 4. Compared with domain 3, the horizontal gradient of water vapor in domain 1 was considerably reduced, and the peak on the left side of the plotted domain almost disappeared. The double-peak structure close to the center became a single peak (i.e., Fig. 4a vs. Fig. 4c). Results from domain 2 were somewhat smoothed, but maintained the main structures well. Since many issues about the retrieved refractivity below the boundary layer are not well solved, such as multipath, superrefraction, etc., we will not pay much attention to this boundary layer region.

Comparisons between wet and dry refractivity (Fig. 5) showed that the inhomogeneities of atmospheric refractivity in the lower atmosphere arise primarily from the wet component (also addressed in Healy 2001), even though its maximum value is about half of that from dry refractivity. Similarly, inhomogeneity from wet refractivity dominated that from dry refractivity in the middle troposphere as well. This implies that good representation of moisture in the computed ideal atmosphere was very important to our error study. The assimilation of SSM/I data was used for this purpose.

Three ideal atmospheres were created using a three-domain MM5 simulation and CIRA data (i.e., ideal atmosphere 1 that consists of MM5 domain 1 and CIRA data, ideal atmosphere 2 that consists of MM5 domain 2 and CIRA, etc.). The three ideal atmospheres represent different resolutions of an arbitrary real atmosphere. Following the procedure in Fig. 1a, given any occultation location and plane, errors of retrieved local refractivity using each of these three ideal atmospheres were compared. Two occultation points, dots 1 and 2 in Fig. 3, were selected, and 12 occultation planes (one plane every  $30^\circ$  in azimuth, see dot 1 in Fig. 3a) were specified for each point.

Due to the curvature of the Earth, a ray integrated horizontally from the surface of the Earth reaches the altitude close to the top of the troposphere ( $\sim 10$  km) at a horizontal distance of about 400 km from its tangent point. To simplify the approach, the occultation points chosen for experiments in this study were within the MM5 domain and away from the

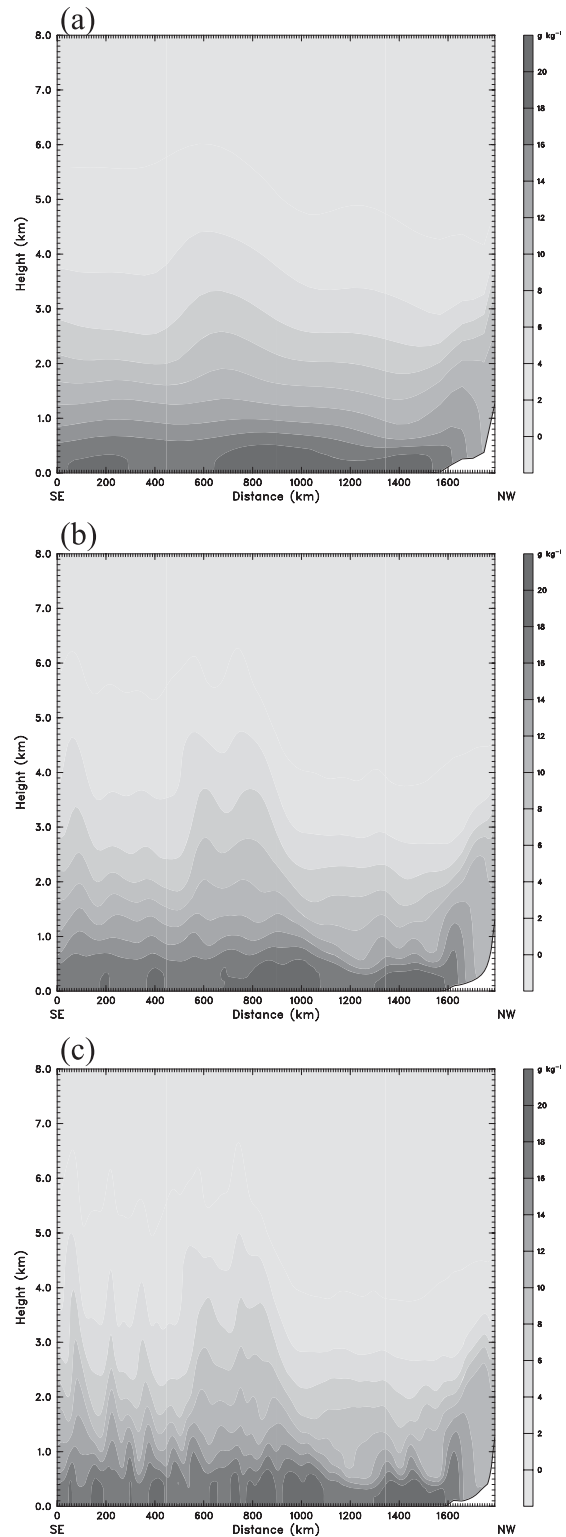


Fig. 4. MM5 24-h simulated vertical cross sections of water vapor mixing ratio ( $\text{g kg}^{-1}$ ) for domains (a) 1, (b) 2, and (c) 3 along the EW lines in Figs. 3a, b, and c, respectively.

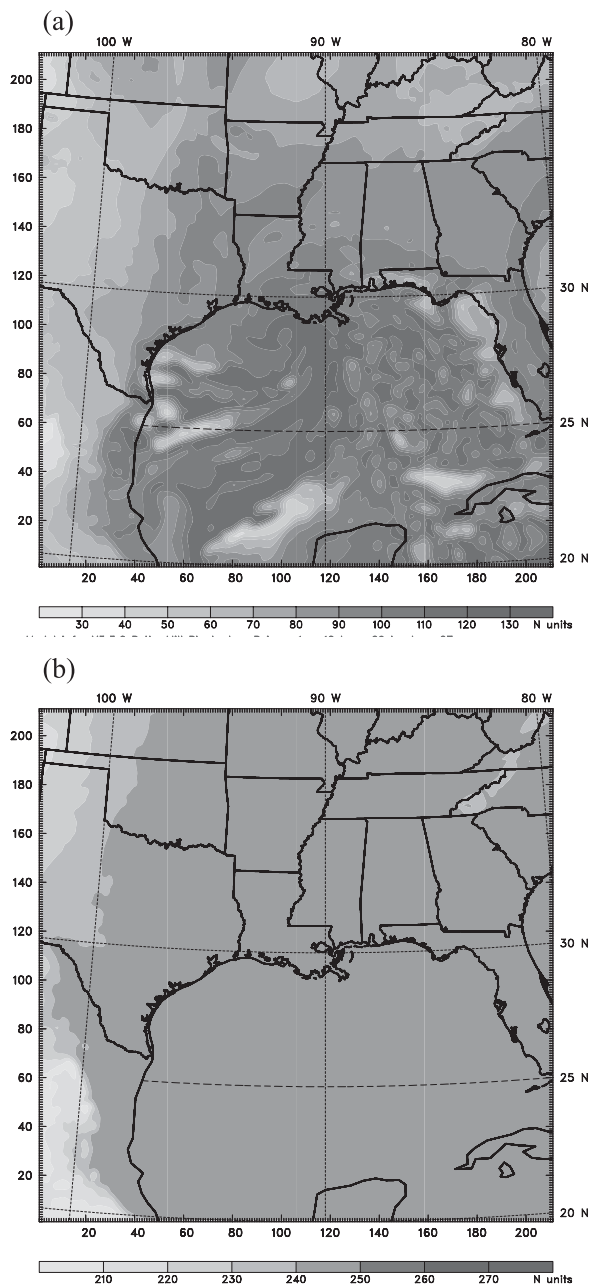


Fig. 5. MM5 24-h simulated (a) wet and (b) dry refractivity at 950 hPa from domain 3, experiment 1. The interval of gray scales is 10 units.

lateral boundary so that rays do not exit MM5 domains into CIRA through its lateral, but rather its upper boundary. At this height, rays exit MM5 almost vertically and therefore, the horizontal gradient, which is the primary error

of the Abelian retrieval algorithm, was no longer an issue.

### 3.1.b. Results

In general, the refractivity was about 300 to 400 units in the lower troposphere, and exponentially decreased to 50 to 100 units in the upper troposphere. Errors of retrieved local refractivity (i.e.,  $N_r - N_i$ ) for each occultation point at each occultation plane were calculated (Fig. 6). At occultation point 1 (column 1), the retrieved refractivity was underestimated in almost the whole column (Figs. 6a, c, and e), while at point 2, the errors changed sign with height (Figs. 6b, d, and f). It is interesting to note that the estimated errors from 12 occultation planes were different in both magnitude and vertical distribution. Unfortunately, this valuable information (i.e., the differences in different occultation directions) cannot be included in the assimilation of retrieved local refractivity, while it can in the bending angle or nonlocal refractivity. Compared with ideal atmosphere 3, the features of the refractivity error from ideal atmosphere 2 were considerably closer than those from ideal atmosphere 1, although the magnitudes are slightly underestimated. This can also be seen in the average and standard deviation of errors from those 12 occultation planes in Fig. 7. Ideal atmosphere 2 can reproduce both the magnitudes and the levels of local maxima and minima reasonably well, such as the double peaks in the lower atmosphere in Figs. 7a and b.

The largest error of retrieved local refractivity from both columns (i.e., points 1 and 2 in Fig. 3) is located in the lower troposphere, and this can have a strong affect on assimilation results (e.g., temperature, moisture, and pressure, etc.) through the use of the observation operator (i.e., Eq. 1). An a joint sensitivity test of refractivity was conducted using the input data from the vertical profile of refractivity ( $N_i$ ), moisture, temperature, and pressure at point 1 from ideal atmosphere 3 (Fig. 3c), and the results are shown in Fig. 8. Refractivity was most sensitive to water vapor, in particular in the lower troposphere, followed by temperature. In other words, compared with temperature and pressure, the unit perturbation, or error, of water vapor in the lower atmosphere will result in the biggest change of refractivity.

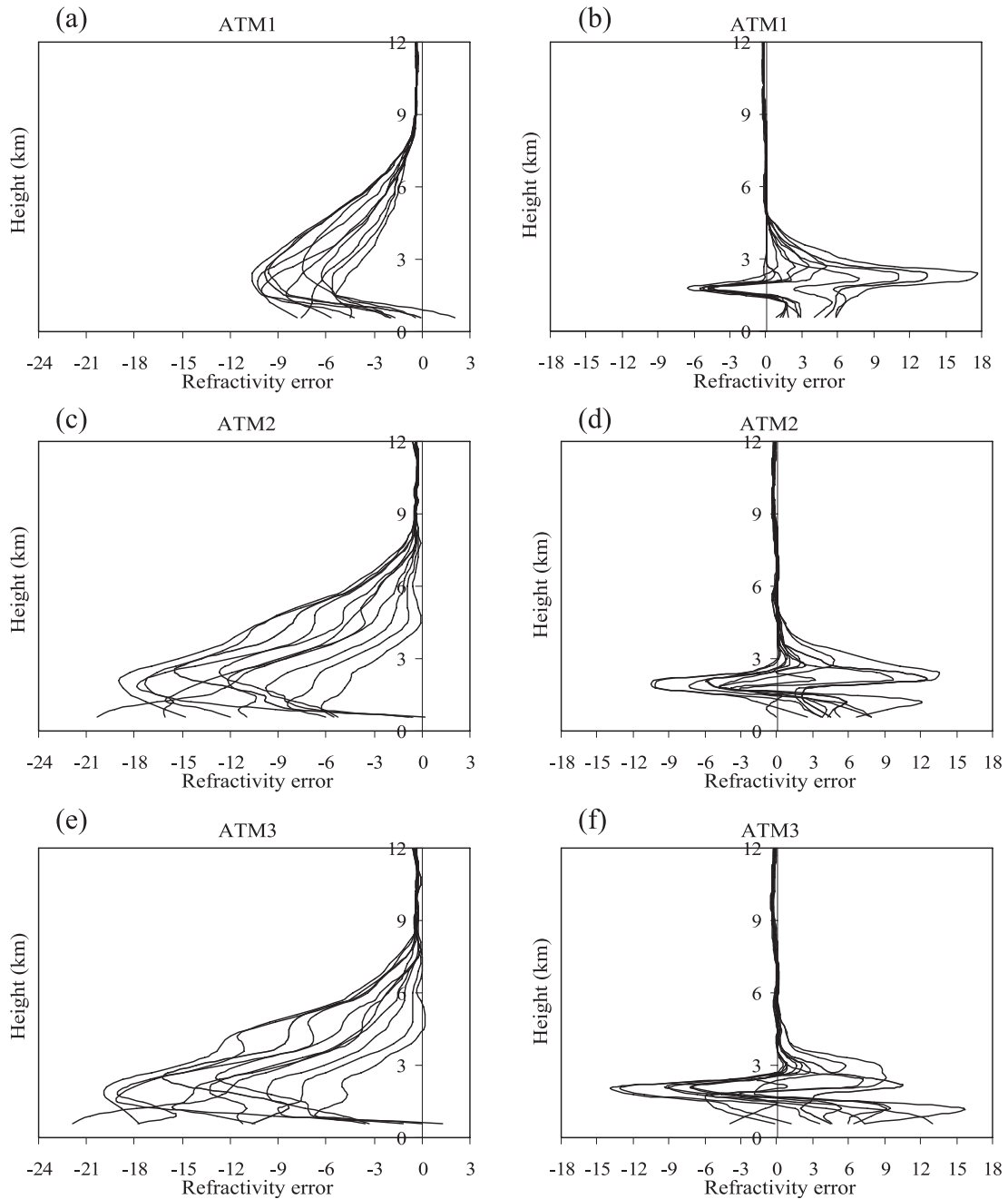


Fig. 6. Errors (differences) of retrieved local refractivity from that computed from ideal atmospheres for 12 occultation planes for points 1 (left column) and 2 (right column) in experiment 1. ATM1–3 denote results from ideal atmospheres 1–3, respectively.

The differences of refractivity computed from three ideal atmospheres ( $N_i$ ), which are treated as an arbitrary real atmosphere in different resolutions, are plotted in Fig. 9. The differ-

ences between ideal atmospheres 2 and 3 are much smaller than those between ideal atmospheres 1 and 3, in particular in the lower atmosphere, where the accuracy of retrieved local

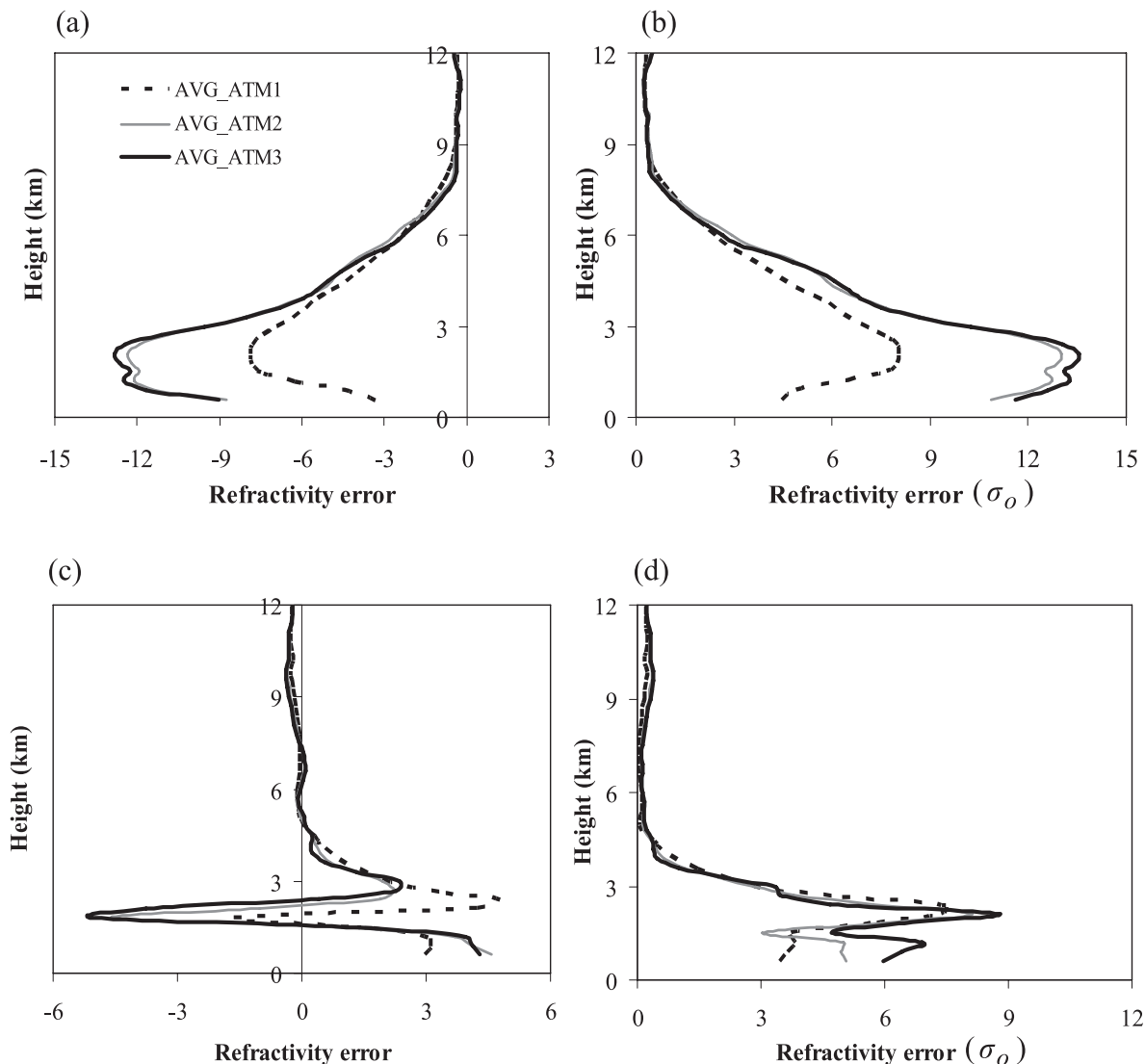


Fig. 7. Averaged errors of the retrieved local refractivity from the 12 profiles in Fig. 6 for points (a) 1 and (c) 2. (b) and (d) are the corresponding standard deviation of (a) and (c), respectively. AV-G\_ATM1–3 denote averaged results from ideal atmospheres 1–3, respectively.

refractivity ( $N_r$ ) is usually a major concern. It should also be noted that the difference at about 2 km of column 2, from the ideal atmosphere 2, is still large (i.e., Fig. 9b). Given the limits of computer resources and the evidence of convergence (i.e., error estimation from atmospheres 2 and 3 are in reasonable agreement), a horizontal spatial resolution higher than 30 km is considered to be reasonable. Thus, a resolution of 20 km should be sufficient for representing the local distribution of water

vapor, which can dominate the refractivity change in this experimental area, and is used in error estimation in the next experiment. A similar resolution of 12 km was used in the simulation study of Healy (2001).

### 3.2 Experiment 2: Estimation of error variances of retrieved refractivity

#### 3.2.a. Experiment design

In experiment 2, a systematic evaluation of errors of retrieved local refractivity ( $N_r$ ) was

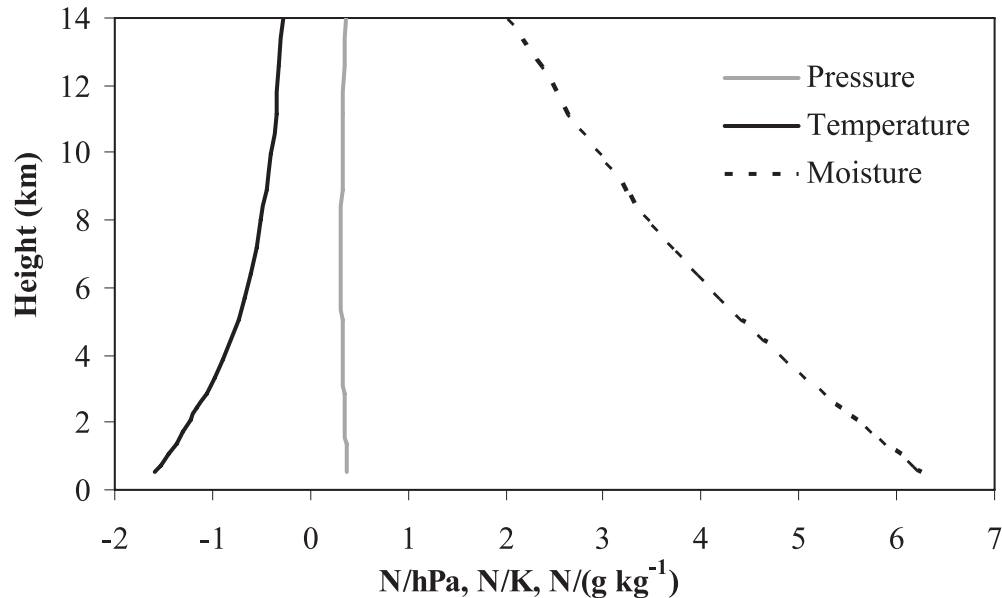


Fig. 8. The vertical profile of the adjoint sensitivity for the total refractivity ( $N_i$ ) with respect to pressure ( $dN_i/dP$ ), temperature ( $dN_i/dT$ ), and moisture ( $dN_i/dq$ ) at point 1 in Fig. 3c, where  $q$  is water vapor mixing ratio.

conducted. Two cases are examined: one is Hurricane Danny, which occurred in the summer of 1997, the same as that in Section 3.1, and the other is a severe winter storm event which was associated with a cyclone that occurred in early February 1998. A single domain MM5 model was used. The model configuration and total integration time (i.e., 24 h) for both cases are the same as those in Section 3.1, except for the model resolution (20 km), time interval (60 s), and grid dimensions ( $271 \times 271 \times 31$  in  $x$ - $y$ - $\sigma$  directions, respectively). The summer and winter cases were integrated for 24 hours from 0000 UTC 17 July 1997 and 0000 UTC 31 January 1998, respectively. SSM/I brightness temperatures were also assimilated in both cases at the initial time.

Figure 10 shows the refractivity at 1 km and 2 km height after 24 h simulations for both 1997 and 1998 cases. The refractivity in summer is higher than in winter and is higher at lower latitudes than at higher latitudes due to the variation in the water vapor content. In addition, high refractivity can be found at locations that are often associated with weather phenomena such as hurricanes and fronts. The ideal atmospheres in this experiment again

consist of a high-resolution MM5 simulation and CIRA data. For each case, 70 occultation points were chosen (Figs. 10a and c) and 6 occultation planes were specified for each point (i.e., one plane every  $60^\circ$  in azimuth; Fig. 10a). This makes a total of 840 retrieved refractivity profiles. The geophysical regions were roughly divided into land (black dots), ocean (white dots), and coastal regions (open circles). The errors were then estimated using the procedure described in Fig. 1a.

### 3.2.b. Results

Figure 11 shows the vertical distribution of the standard deviation of retrieved local refractivity errors ( $\sigma_o$ ). The errors from the 1997 summer case (thick gray-solid line) are larger than those from the 1998 winter case (thick gray-dashed line), due to the high water content in summer. Similar results were also obtained by Kuo et al. (2004) and Rocken et al. (1997). Despite the difference in magnitude, vertical profiles from both seasons are very similar. Larger errors are concentrated at the lower atmosphere due to the high water vapor content and its vertical and horizontal gradient. The error decreases with height, meander-

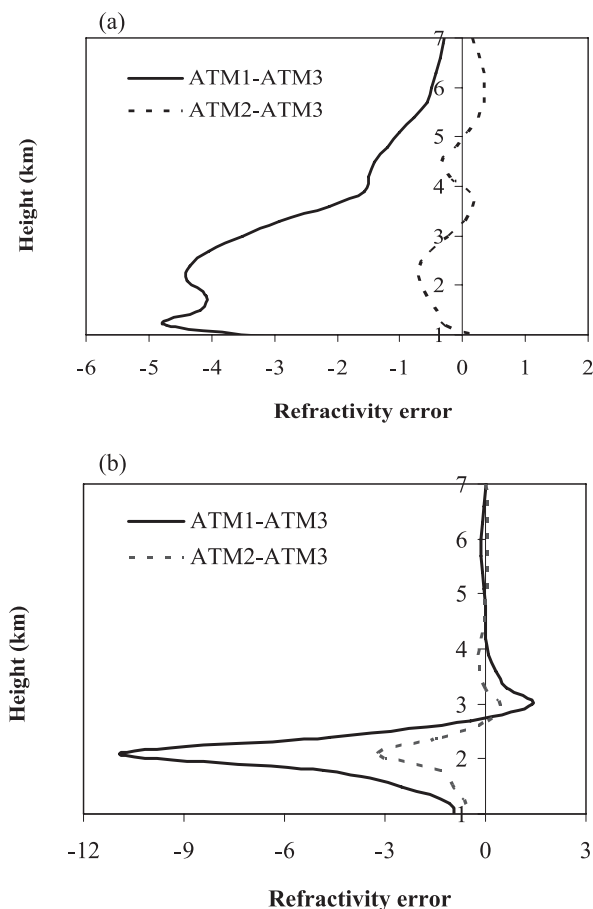


Fig. 9. Differences of computed refractivity ( $N_i$ ) between ideal atmosphere 1 and 3 (ATM1-ATM3; solid lines) and between ideal atmosphere 2 and 3 (ATM2-ATM3; dashed line) for point (a) 1 and (b) 2 in Fig. 3.

ingly in the first 3 km, and more rapidly in the rest of the atmosphere. This meandering feature was not obtained by Kuo et al. (2004), who used real GPS observations and coarse global reanalysis. Since the errors below and above 3 km are quite different, curve fittings (thin black-solid line) for these two regions were calculated individually using data from both cases (thick black-solid line). The formulae of the standard deviation,  $\sigma_o$ , are:

$$\sigma_o = \begin{cases} 88.3z^{-2.31} & z \geq 3 \text{ km} \\ -0.75z + 8.5 & z < 3 \text{ km} \end{cases}$$

where  $z$  is the height in units of km. The error above 7 km is slightly less than 1.5 units (Fig.

11). The quality of retrieved local refractivity is considerably higher above this level. If computational resources and time are not restricted, a combination of assimilating the retrieved local refractivity in the upper atmosphere and the bending angle or non-local refractivity in the lower atmosphere could be a good approach. A height of 6 to 7 km is a good separating level. This is consistent with results from Zou et al. (1999).

The errors of retrieved local refractivity over ocean, land, and coastal regions are plotted in Fig. 12. Results from both cases are quite consistent (Figs. 12b and c). The altitude of the maximum error over land is about 2–3 km, which is higher than that over the ocean ( $\sim 1$  km). Both seem closely related to the heights of the boundary layer where the moisture gradient is large. The combined effect of these two regions explains the meandering feature of error below 3 km in Fig. 11. The maximum error over ocean is close to the surface, due to a shallow inhomogeneous moist boundary layer, while the higher altitude of the maximum error over land might be due to a deeper inhomogeneous moist boundary layer and complex topography. As a result, the magnitude of the error over ocean in the lower troposphere is higher than over land, due to the height difference of these two maximum error levels. Both cases in Fig. 12 consistently show that the quality of retrieved local refractivity over ocean is slightly better than that over land between approximately 2 km and 4 km, indicating a smaller horizontal moisture gradient in this layer over ocean than over land. In the coastal region, the meandering feature is also evident below the 3 km height, as a combined effect of the errors over land and ocean. From these results one can infer that different vertical profiles of error variances might be required over ocean, land, and coastal regions in order to better assimilate retrieved local refractivity.

A local maximum error noticed around 6-km height for the 1997 case (Fig. 11) appears to be due to the land, as shown in Fig. 12b. The plot of refractivity ( $N_i$ ) at 6 km height (Fig. 13) shows that there exist strong disturbances, which introduce large refractivity as well as inhomogeneity, on the lee side of the Rockies. The error at this altitude (i.e.,  $\sim 6$  km) over this disturbance region and in its vicinity is higher

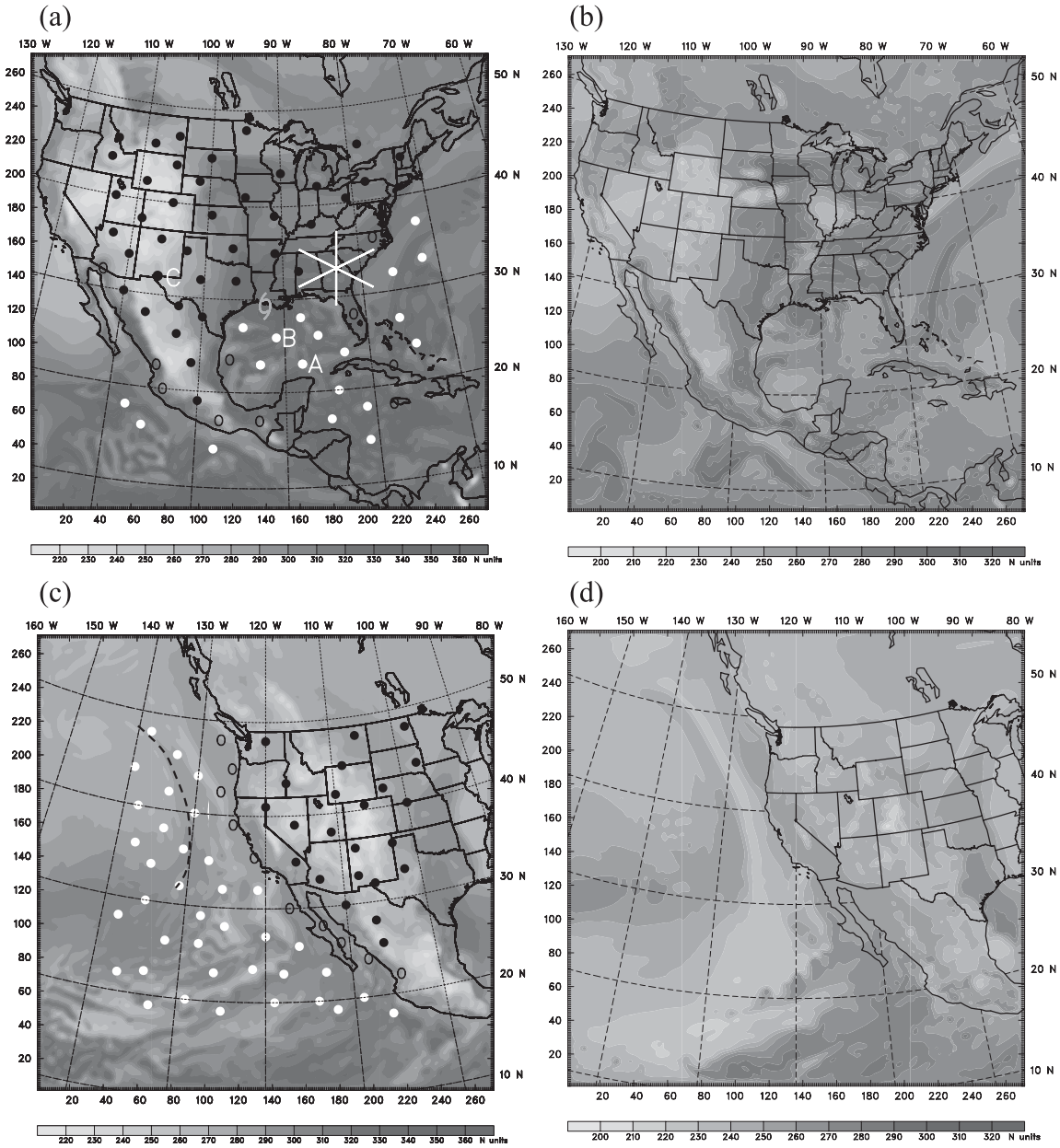


Fig. 10. MM5 24-h simulated refractivity at 1 km height for (a) 1997 and (c) 1998 cases and 2 km height for (b) 1997 and (d) 1998 cases from experiment 2. Seventy occultation points shown in (a) and (c) from each case are selected and 6 occultation planes (i.e., every 60°; see (a)) are specified for each point to estimate error variances (or the standard deviation) of retrieved local refractivity. Three geophysical regions are distinguished: land (black dots), ocean (white dots) and coastal regions (open circles). The hurricane symbol in (a) denotes the location of Danny. The dashed line in (c) indicates the position of the front which is associated with a cyclone.

than others (see the gray solid line shown in Fig. 14).

As mentioned earlier, the altitude of the maximum error of retrieved local refractivity over

the ocean is approximately at a height of 1 km (black solid line in Fig. 14). However, the level of the maximum error can be shifted to higher levels (dashed line vs. black solid line in Fig.

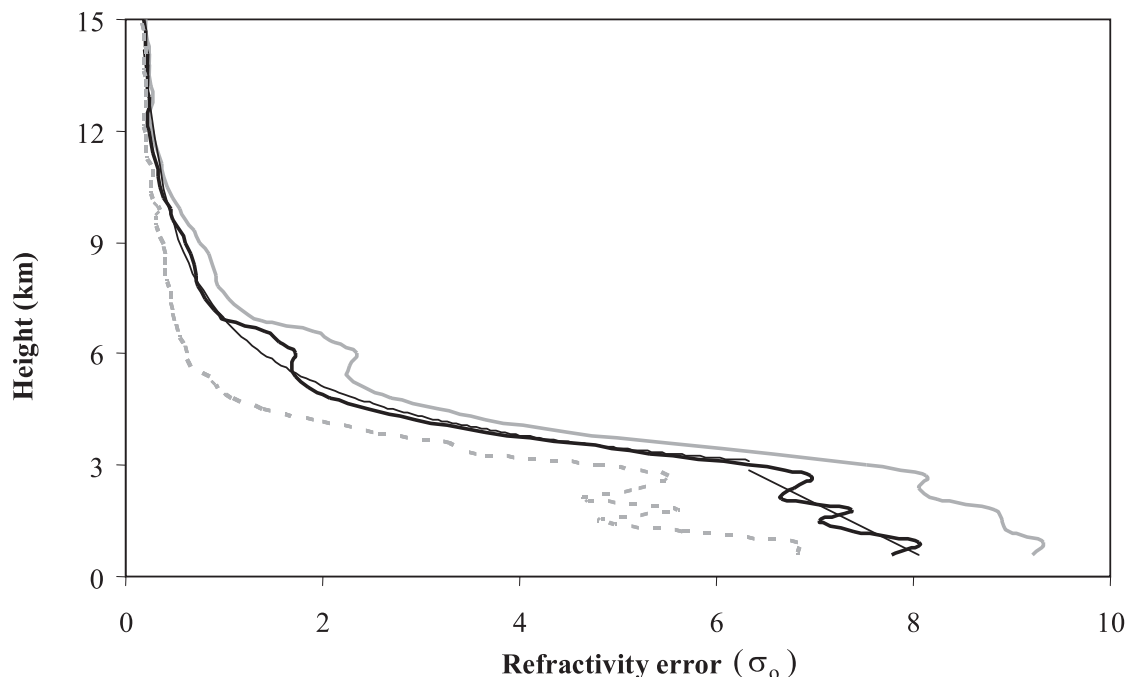


Fig. 11. Standard deviation of retrieved local refractivity error ( $\sigma_0$ ) from 1997 case (thick gray-solid line), 1998 case (thick gray-dashed line), and both (thick black-solid line). The thin black-solid line is the result from curve fitting for both cases. The regression formulae for the fitted curves above and below 3 km are  $\sigma_0 = 88.3z^{-2.31}$  and  $\sigma_0 = -0.75z + 8.5$ , respectively, where  $z$  is the height in km.

14) when the shallow boundary layer is expanded or disappears due to the existence of disturbances, such as cyclones or hurricanes.

Using radiosondes and global reanalysis, Kuo et al. (2004) showed that errors of the local refractivity retrieved from the observed GPS occultation data at lower latitudes are greater than those at higher latitudes. To compare their results with those of this study, the averaged standard deviation errors, to the north and south of  $30^\circ\text{N}$ , were plotted separately for both cases (Fig. 15). Errors at the higher latitude (i.e.,  $>30^\circ\text{N}$ ) are smaller than those at the lower latitude, in particular in the middle troposphere and the boundary layer, due to the high water vapor content. However, it is also found that the errors between 1.5 km and 3 km are in fact comparable from these two regions for both cases. The vertical profile of the error at the higher latitude from the 1997 case (black line in Fig. 15a) is very similar to that over land (black solid line in Fig. 12a) since al-

most all occultation points are over land (Fig. 10a).

### 3.3 Experiment 3: Sensitivity test of model resolution to error variances of retrieved local refractivity

#### 3.3.a. Experiment design

The assimilation of retrieved local refractivity can improve model simulations/forecasts when the numerical model resolution is relatively coarse ( $\sim 300$  km; Anthes et al. 2000). This approach is also proven to have a positive impact on reducing analysis and forecast temperature error in the upper troposphere and lower stratosphere with a higher model resolution ( $\sim 60$  km; Healy et al. 2005). Sokolovskiy et al. (2005) investigated the effect of horizontal resolution of an atmospheric model on the errors of modeling local and nonlocal linear radio occultation observables. For the local refractivity, they concluded that the observation errors are dominated by the observation modeling er-

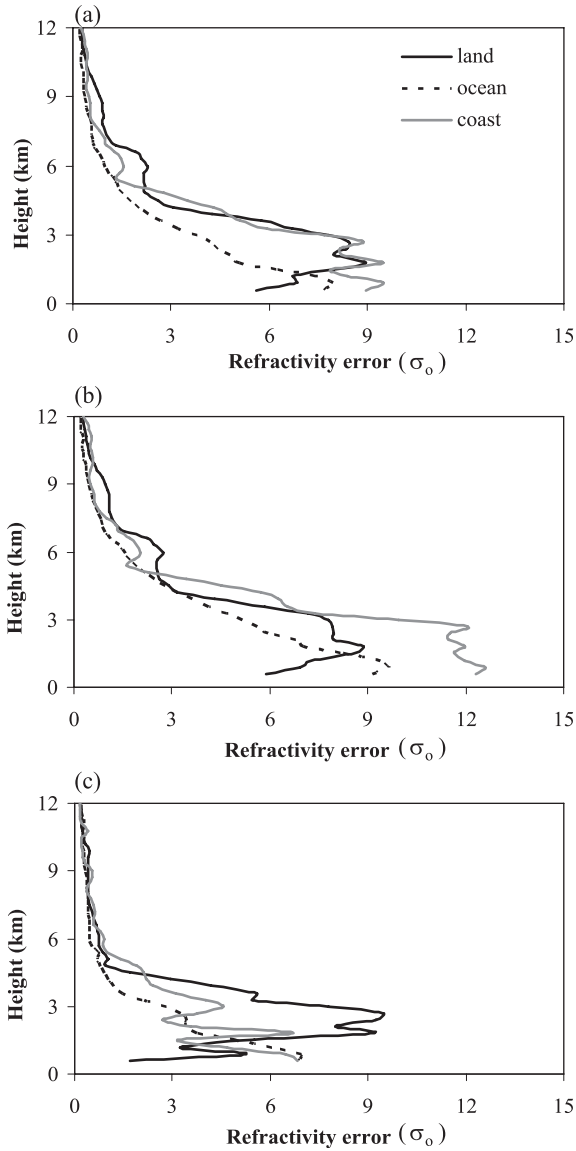


Fig. 12. Standard deviation of retrieved local refractivity error ( $\sigma_0$ ) over land (black-solid line), ocean (black-dashed line), and coast (gray-solid line) for (a) both, (b) 1997, and (c) 1998 cases.

rors for a high-resolution model, and by the model representativeness errors for a low-resolution model; the errors are minimized at a resolution of about 300 km. Here, experiment 3 was designed to revisit the observation errors with respect to different model horizontal resolutions when modeling retrieved local refractivity.

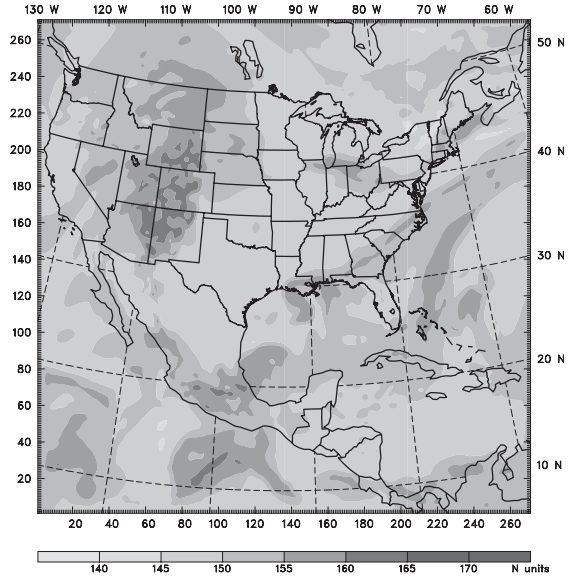


Fig. 13. MM5 24-h simulated refractivity at 6 km for the 1997 case from experiment 2.

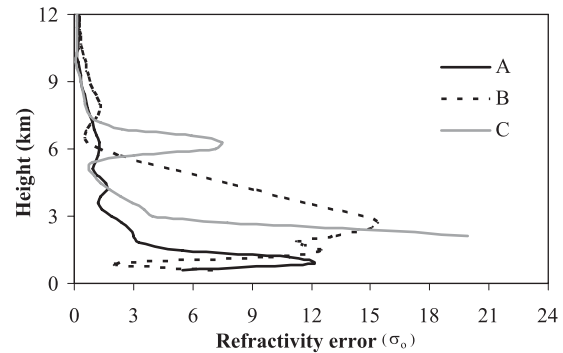


Fig. 14. Standard deviation of retrieved local refractivity error ( $\sigma_0$ ) for points A (black solid line), B (dashed line), and C (gray solid line) for the 1997 case in Fig. 10a. Each profile is calculated from 6 occultation planes that are specified for each point (i.e., one plane every  $60^\circ$  in azimuth).

Retrieved local refractivity profiles ( $N_r$ ) from ideal atmosphere 3 in experiment 1 (i.e., MM5 domain 3 with a resolution of 10 km plus CIRA data) were used as true observables. When modeling retrieved local refractivity, different model horizontal resolutions were achieved by taking the average over various numbers of

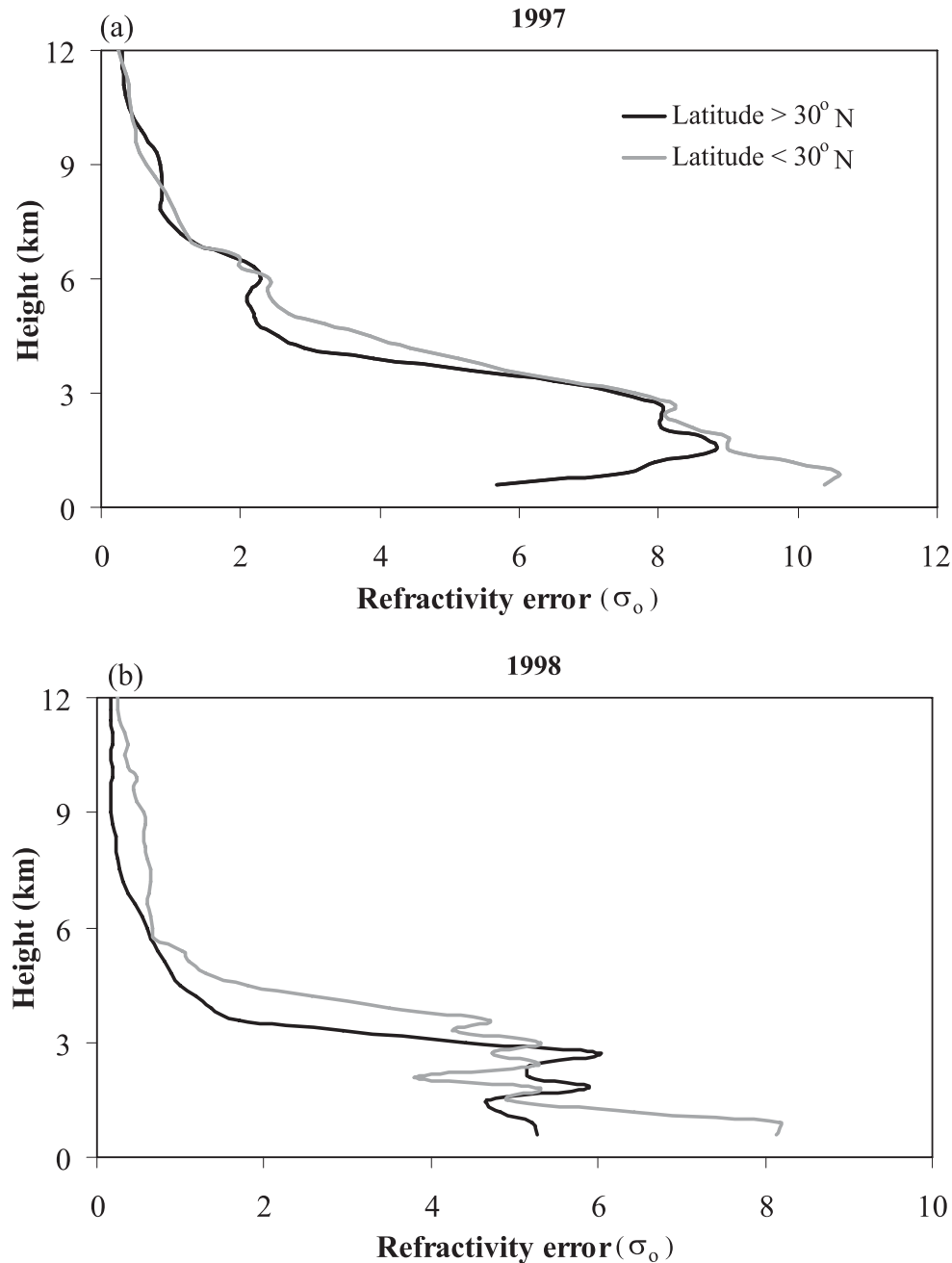


Fig. 15. Standard deviation of retrieved local refractivity error ( $\sigma_0$ ) above (black lines) and below (gray lines)  $30^\circ$ N for (a) 1997, and (b) 1998 cases.

grid boxes. For example, the 90-km resolution  $N_i$  was obtained by averaging  $9 \times 9$  grid boxes with the occultation point located within the central box. To avoid the problem of averaging grid boxes that have different elevations of topography in the lower troposphere, 7 occulta-

tion points over ocean were chosen (Fig. 3c). For each occultation point, 6 occultation planes (i.e., every  $60^\circ$ ) were specified, as in experiment 2. The observation errors with respect to different model resolutions were then calculated and compared.

### 3.3.b. Results

Figure 16 shows the error of retrieved local refractivity with respect to different model resolutions. When the resolution decreases, the error is consistently reduced throughout the whole troposphere. This implies that when local refractivity data are assimilated, different vertical profiles of error variances should be considered according to model resolutions of the background (i.e., first guess). For example, for a resolution of 250 km, the formula of the standard deviation,  $\sigma_o$ , over ocean for those points in Fig. 16 is  $\sigma_o \approx 9 \exp(-0.306z)$ , where  $z$  is the height in units of km (an exponential formula is often used). However, with a resolution of 20 km, a polynomial,

$$\sigma_o \approx 3 \times 10^{-4}z^4 - 1.54 \times 10^{-2}z^3 + 3.24 \times 10^{-1}z^2 - 2.92z + 9.86,$$

instead of an exponential formula better fits results over ocean for both the 1997 and 1998 cases (dashed line in Fig. 12a).

As expected, there exists an optimal resolution for minimizing error variances of retrieved local refractivity. However, it is noticed that the error reaches a minimum or starts increasing when the resolution is coarser than about 190 km in the lower troposphere and about 250 km in the middle to upper troposphere. The optimal resolution in the lower troposphere (i.e.,  $\sim 190$  km) is higher than in the middle to upper troposphere (i.e.,  $\sim 250$  km) due to the stronger vertical gradient of refractivity and the higher vertical resolution in the lower troposphere (Kursinski et al. 1997).

It is interesting to note that the meandering feature is evident in the results over ocean in Fig. 16. This is because some sampling points are close to Hurricane Danny and the boundary layer is either deeper or disappears as discussed earlier (dashed line in Fig. 14). It is also interesting to note that after smoothing the data with other regular ocean points (i.e., a coarser model resolution) the meandering feature almost disappears.

As mentioned earlier, the meandering feature of error over land was not obtained by Kuo et al. (2004). This may be due to the use of a coarse-resolution global reanalysis data-set in their study, for which the horizontal gradient of refractivity is significantly reduced after smoothing.

## 4. Concluding remarks

This simulation study was designed to study error characteristics of retrieved local refractivity. The ray-tracing code based on Zou et al. (1999), which was applied to global reanalysis, is adapted to a regional model in this study. To better estimate errors caused by the spherical symmetry assumption, a high resolution MM5 simulation in the lower atmosphere, along with CIRA climate data elsewhere, was used as an ideal atmosphere. Using this ideal atmosphere, the ray tracing code was applied to simulate bending angles, which were then used to retrieve refractivity using the Abelian algorithm (see flow chart in Fig. 1a).

The convergence of error estimation with respect to different model resolutions was first examined using MM5 simulations. In this study, the results converged reasonably when the resolution was higher than 30 km. The maximum errors were found to be located in the lower troposphere, as in other studies. From an adjoint sensitivity test, the error of refractivity was determined to be most sensitive to the low-level moisture, and, to a lesser extent, the low-level temperature field. It is worth pointing out that when different azimuth angles are specified for the same occultation point, the discrepancy of retrieved errors with respect to different azimuth angles (i.e., different occultation planes) is non-negligible. Unfortunately, this valuable information is not included in the assimilation of retrieved local refractivity, but rather in the bending angle or non-local refractivity.

Two cases were chosen to study error characteristics of retrieved local refractivity: one is from the summer hurricane season in 1997 and the other is a winter cyclone in 1998. The uncertainty of retrieved refractivity can reach 10 units in the lower troposphere under the assumption of spherical symmetry. The error of retrieved local refractivity decreases with height linearly up to a height of about 3 km, and then more rapidly above that height. The error is considerably smaller at elevations higher than about 7 km, which is a good separation level when one wishes to assimilate different products in different regions (e.g., retrieved local refractivity above 7 km and bending angles below). A local maximum in the

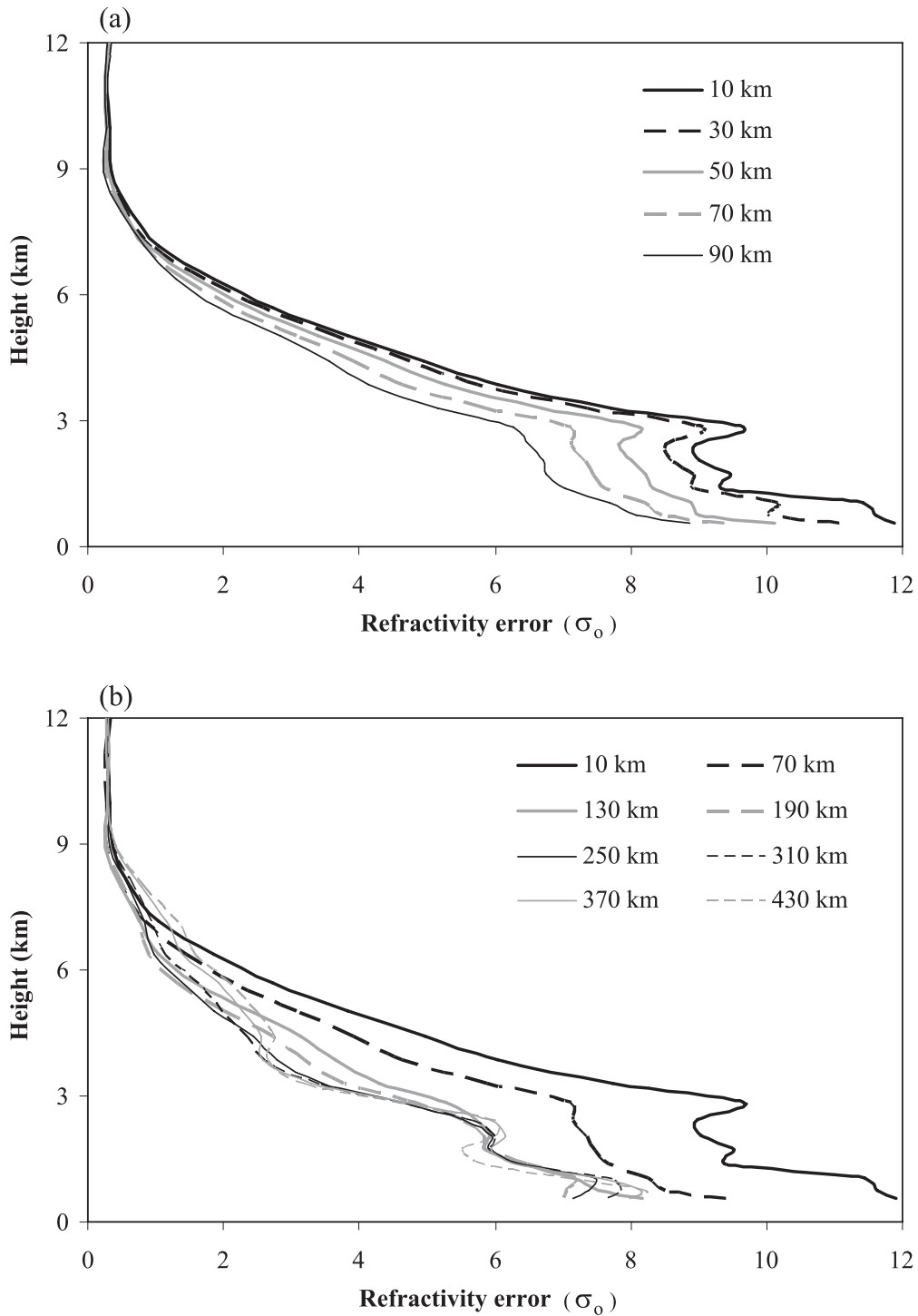


Fig. 16. Standard deviation of retrieved local refractivity error ( $\sigma_0$ ) with different model resolutions from 7 points in Fig. 3c. Different resolutions are obtained by taking the average of different numbers of grid boxes from the ideal atmosphere (see text for detail).

error at about 6 km, found for the 1997 case, is due to large refractivity disturbances on the lee side of the Rockies around that height.

Due to the amount and the variation in the water vapor content, the error of retrieved refractivity in the summer is higher than in the winter and is higher at lower latitudes than at higher latitudes, as shown in previous studies (Kuo et al. 2004). It was also found that the level of the maximum error over land ( $\sim 2\text{--}3$  km) is higher than over the ocean ( $\sim 1$  km), and this is possibly due to the complex topography and deeper boundary layer over land. The combined effect of these two regions produces a meandering feature of error variances below 3 km. The error at heights close to the surface over the ocean is slightly worse than that over the land; however, it is slightly better than that over land between approximately 2 km and 4 km, indicating smaller horizontal moisture gradients in this layer over the ocean. The altitude of maximum error over the ocean can be shifted upward when strong disturbances, such as severe weather, occur over the region.

When modeling observations, unlike point observations (i.e., in-situ data) whose error increases when the model resolution decreases, the observation error of retrieved local refractivity is reduced with a decrease in model resolution (Sokolovskiy et al. 2005), and there exists a lower limit in the optimal resolution. The optimal value is smaller in the lower troposphere ( $\sim 190$  km) than in the middle and upper troposphere ( $\sim 250$  km), and this difference exists because of the strong vertical gradient of refractivity and higher vertical resolutions in the lower troposphere (Kursinski et al. 1997).

The results obtained from this study are quite interesting. Due to the assumption of spherical symmetry in the Abelian inversion algorithm, and the amount and the variation of water vapor content, the vertical profiles and magnitudes of retrieved local refractivity error highly depend on the location (i.e., land vs. ocean and high vs. low latitude), season, flow pattern (i.e., disturbances in the atmosphere), and model resolution. This implies that when local refractivity is assimilated, different error variances may be considered under different conditions. For example, when modeling local refractivity over ocean an exponential relationship between the standard deviation and height can be ap-

plied to a coarser model resolution, while a polynomial function may be more appropriate for a high model resolution. It is expected that if the retrieved refractivity data are utilized properly, according to their error characteristics, their impact on reanalysis can be optimized.

### Acknowledgements

The SSM/I data were provided by the Global Hydrology Resource Center at the Global Hydrology and Climate Center, NASA, Huntsville, Alabama. This study is partially sponsored by Taiwan FORMOSAT-3 project.

### References

- Anthes, A.R., C. Rocken, and Y.-H. Kuo, 2000: Applications of COSMIC to meteorology and climate. *Terr. Atmos. Ocean Sci.*, **11**, 115–156.
- Chen, S.-H., F. Vandenberghe, G.W. Petty, and J.F. Bresch, 2004: Application of SSM/I satellite data to a hurricane simulation. *Quart. J. Roy. Meteor. Soc.*, **130**, 801–825.
- Eyre, J.R., 1994: Assimilation of radio occultation measurements into a numerical weather prediction system. ECMWF Tech. Memo., 199, Reading, UK.
- Grell, G.A., J. Dudhia, and D.R. Stauffer, 1994: A description of the fifth-generation Penn State/NCAR mesoscale model (MM5). NCAR/TN-398+STR, National Center for Atmospheric Research, Boulder, CO, 122 pp.
- Hajj, G.A., E.R. Kursinski, L.J. Romans, W.I. Bertiger, and S.S. Leroy, 2002: A technical description of atmospheric sounding by GPS occultation. *J. Atmos. Sol. Terr. Phys.*, **64**, 451–469.
- Healy, S.B. and J.R. Eyre, 2000: Retrieving temperature, water vapour and surface pressure information from refractive-index profiles derived by radio occultation: a simulation study. *Quart. J. Roy. Meteor. Soc.*, **126**, 1661–1683.
- , 2001: Radio occultation bending angle and impact parameter errors caused by horizontal refractive index gradients in the troposphere: A simulation study. *J. Geophys. Res.*, **106**, D11, 11875–11889.
- , A.M. Jupp, and C. Marquardt, 2005: Forecast impact experiment with GPS radio occultation measurements. *Geophys. Res. Lett.*, **32**, L03804 10.1029/2004GL020806.
- Hollingsworth, A. and P. Loennberg, 1986: Statistical structure of short-range forecast errors as determined from radiosonde data, Pt. 1: The wind field. *Tellus*, **38**, 111–136.
- Huang, C.-Y., Y.-H. Kuo, S.-H. Chen, and F. Vandenberghe, 2005: A comparison of SSM/I and

- berghe, 2005: Improvements on typhoon forecast with assimilated GPS occultation refractivity. *Wea. Forecasting*, in press.
- Kuo, Y.-H., X. Zou, and W. Huang, 1997: The impact of Global Position System data on the prediction of an extratropical cyclone: An observing system simulation experiment. *J. Dyn. Atmos. Ocean*, **27**, 439–470.
- , S.V. Sokolovskiy, R.A. Anthes, and F. Vandenberghe, 2000: Assimilation of GPS radio occultation data for numerical weather prediction. *Terr. Atmos. Ocean Sci.*, **11**, 157–186.
- , T.K. Wee, S. Sokolovskiy, C. Rocken, W. Schreiner, D. Hunt, and R.A. Anthes, 2004: Inversion and error estimation of GPS radio occultation data. *J. Meteor. Soc. Japan*, **82**, 507–531.
- Kursinski, E.R., G.A. Hajj, J.T. Schofield, R.P. Linfield, and K.R. Hardy, 1997: Observing Earth's atmosphere with radio occultation measurements using the Global Positioning System. *J. Geophys. Res.* **102**, D19, 23429–23465.
- Liu, H. and X. Zou, 2003: Improvements to a GPS radio occultation ray-tracing model and their impacts on assimilation of bending angle. *J. Geophys. Res.* **108**, D17, 10.1029/2002JD003160.
- Loennberg, P. and A. Hollingsworth, 1986: Statistical structure of short-range forecast errors as determined from radiosonde data, Pt. 2: Covariance of height and wind errors. *Tellus*, **38**, 137–161.
- Palmer, P.I., J.J. Barnett, J.R. Eyre, and S.B. Healy, 2000: A nonlinear optimal estimation inverse method for radio occultation measurements of temperature, humidity, and surface pressure. *J. Geophys. Res.*, **105**, D13, 17513–17526.
- Poli, P., J. Joiner, and E.R. Kursinski, 2002: 1DVAR analysis of temperature and humidity using GPS radio occultation refractivity data. *J. Geophys. Res.*, **107**, D20, 10.1029/2001JD000935.
- and ———, 2004: Effects of horizontal gradients on GPS radio occultation observation operators. I: Ray tracing. *Quart. J. Roy. Meteor. Soc.*, **130**, 2787–2805.
- Rocken, C., R. Anthes, M. Exner, D. Hunt, S. Sokolovskiy, R. Ware, M. Gorbunov, W. Schreiner, D. Feng, B. Herman, Y.-H. Kuo, and X. Zou, 1997: Analysis and validation of GPS/MET data in the neutral atmosphere. *J. Geophys. Res.*, **102**, D25, 29849–29866.
- Seemann, S.W., J. Li, W.P. Menzel, and L.E. Gumley, 2003: Operational retrieval of atmospheric temperature, moisture, and ozone from MODIS infrared radiances. *J. Appl. Meteor.* **42**, 1072–1091.
- Sokolovskiy, S., Y.-H. Kuo, and W. Wang, 2005: Assessing the accuracy of a linearized observation operator for assimilation of radio occultation data: Case simulations with a high-resolution weather model. *Mon. Wea. Rev.*, **133**, 2200–2212.
- Syndergaard, S., E.R. Kursinski, B.M. Herman, E.M. Lane, and D.E. Flittner, 2005: A refractive index mapping operator for assimilation of occultation data. *Mon. Wea. Rev.*, **133**, 2650–2668.
- Xu, Q., L. Wei, A. Van Tuyl, and E.H. Barker, 2001: Estimation of three-dimensional error covariances. Part I: Analysis of height innovation vectors. *Mon. Wea. Rev.*, **129**, 2126–2135.
- and ———, 2001: Estimation of three-dimensional error covariances. Part II: Analysis of wind innovation vectors. *Mon. Wea. Rev.*, **129**, 2939–2954.
- Zou, X., Y.-H. Kuo, and Y.-R. Guo, 1995: Assimilation of atmospheric radio refractivity using a non-hydrostatic adjoint model. *Mon. Wea. Rev.*, **123**, 2229–2249.
- , F. Vandenberghe, B. Wang, M.E. Gorbunov, Y.-H. Kuo, S. Sokolovskiy, J.C. Chang, J.G. Sela, and R.A. Anthes, 1999: A ray-tracing operator and its adjoint for the use of GPS/MET refraction angle measurements. *J. Geophys. Res.*, **104**, D18, 22301–22318.
- , B. Wang, H. Liu, R.A. Anthes, T. Matsu-mura, and Y.-J. Zhu, 2000: Use of GPS/MET refraction angles in three-dimensional variational analysis. *Quart. J. Roy. Meteor. Soc.* **126**, 3013–3040.
- , H. Liu, and R.A. Anthes, 2002: A statistical estimate of errors in the calculation of radio-occultation bending angles caused by a 2D approximation of ray tracing and the assumption of spherical symmetry of the atmosphere. *J. Atmos. Oceanic Technol.* **19**, 51–64.